Supplementary Information

for

Tensile strain engineering on Cu nano-dots for high efficiency HMFOR at low potential

Honglei Chen,[a] Yanming Li, [a] Wenbin Ma, [a] Qi Chen, [a] Xupeng Qin,[b] Yitao Liu, [a] Lan Wang,[a,c] Qinghua Liu,[b] Chunzhen Yang,[a]* Changli Li, [a]* Jingfu He[a]*

a. School of Materials, Shenzhen Campus of Sun Yat-sen University, No. 66, Gongchang Road, Guangming District, Shenzhen, Guangdong 518107, P.R. China

b. National Synchrotron Radiation Laboratory, University of Science and Technology of China, Hefei 230029, Anhui, P.R. China

c. School of Chemical Engineering, Sichuan University of Science and Engineering, Zigong 643000, People's Republic of China.

ChunZhen Yang-Email: yangchzh6@mail.sysu.edu.cn

Changli Li* − Email: lichli5@mail.sysu.edu.cn

Jingfu He* − Email: hejf27@mail.sysu.edu.cn

1 Methods

1.1 Materials and chemicals.

Commercial Cu foam was purchased from Canrd Chemical Technology. Potassium hydroxide (analytical reagent, AR), hydrochloric acid (AR), isopropanol, potassium halide, sodium hydroxide, ammonium sulfateacetone and ammonium formate (HPLC) were purchased from Macklin Chemical Reagent. Ethanol and Copper (II) Sulfate Pentahydrate were purchased from General-Ragent Chemical Reagent. 5-Hydroxymethyl-2-furaldehyde, Methanol (HPLC) were purchased from Aladdin Chemical Reagent, 5-Hydroxymethyl-2-furancarboxylic acid were purchased from Bide Chemical Reagent.

1.2 Synthesis of catalysts

1.2.1 Pretreatment of Cu foam (CF)

Copper foam was sonicated with acetone, 3 M HCl, absolute ethanol, and deionized water for 5 min respectively. Then, the cleaned copper foam was blowing dry with nitrogen.

1.2.2 Pretreatment of Carbon paper (CP)

Carbon paper was sonicated with isopropyl alcohol, absolute ethanol, and deionized water for 5 min respectively. Then, the cleaned copper foam was blowing dry with nitrogen.

1.2.3 Synthesis of CuX (X=Cl, Br, I, OH)

Firstly, a 3.6um Cu film was plated on CP by hot evaporation named Cu-CP. Then, a mixed solution of copper halide was prepared (40mL) including $CuSO_4$ 0.1M, H_2SO_4 1M and KX 0.5M. After ultrasonic stirring for 30 minutes, soak CP for 30 minutes, take it out, rinse it with ethanol and water, and blow dry it with nitrogen. CuOH-CP was obtained by soaking Cu-CP in alkaline solution for the same time. The solution formula was that 1.6g NaOH and 0.456g $(NH_4)_2S_2O_8$ were dissolved in 21mL water. After this, we can get CuX-CP. For CF substrate, the halogenation time changed to 5 minutes, and CuX-CF were prepared. Particularly, for the first step of preparation for ID-n%s-Cu (CP), n of 0.49, 2.5, 5.4, 6.4 and 6, corresponding to halogenation duration of 1, 5, 10, 30 and 40 minutes, respectively. For ID-n%s-Cu (CF), the corresponding halogenation time is shortened to 1/6 of CP.

1.2.4 Synthesis of XD-Cu (X=Cl, Br, I, OH)

The XD-Cu was electroreduced by a three-electrode system. The electrolyte was CO_2-satuated 0.1M $KHCO_3$, whose pH was 6.85. The CuX-CF/CP was used as working electrode, AgCl electrode was used as the reference electrode, Pt electrode was used as the counter electrode, the reduction was at -1.1V vs AgCl for 10 minutes.

1.2.5 Synthesis of Cu_2O-Cu

The Cu_2O-CF was synthesized by electrochemical activation. Specifically, the CF was used as working electrode, Hg/HgO electrode was used as the reference electrode, the oxidation was completed under the CV test of the three-electrode system between -0.1 and 1.2 V vs RHE in 1M KOH for 5 cycles at a scan rate of 5 mV/s. After that, the CF that completed activation was soaked in KOH for 13 h. Next,

the sample was reduced at - 0.3 V vs RHE for 600 s. Finally, the obtained Cu_2O-CF was washed with ethanol and dried with nitrogen.

2 Characterization and tests

2.1 Characterization

The morphology and microstructure of all the electrodes were investigated SEM (Hitachi, SU5000). The high-resolution morphology of these materials was observed by TEM (FEI Tecnai G2 F20). XRD was employed on a Rigaku SmartLab SE diffractometer with a Cu Ka source. Diffraction data were collected for 2ɵ from 10 to 90 °. The Raman spectra was recorded at room temperature on a WiTech alpha 300R with an argon ion laser operating at 488 nm. For PDF test, the total scattering patterns (Bragg diffraction patterns and diffuse scattering data) were acquired with two-dimensional (2D) detectors (PZ Medical 6557 a-Si 2D image plates) at the BL13HB beamline of the Shanghai Synchrotron Radiation Facility (SSRF) (40.44 keV beam energies). u2D images were converted into 1D Q-space versus intensity plots by using the Dioptas program with a CeO_2 calibration standard, and PDF patterns (G(r)) were obtained with the PDFgetX3 software. The XPS was performed on an Thermo Scientific K-Alpha X-ray photoelectron spectrometer using Al as the excitation source (hv=1486.6eV). In-situ FT-IR measurements of HMF adsorption was carried out over Bruker infrared spectrometer (Transmission cell) in the reaction cell. The IR reaction cell was equipped without window and a typical three electrodes system was operated (Pt wire as counter electrode and Hg/HgO as reference electrode).

2.2 Electrochemical measurements

The linear sweep voltammetry (LSV) and cyclic voltammetry (CV) was recorded in an H-type electrochemical cell with 1 M KOH and various quantities of HMF at room temperature at a scanning rate of 5 mV/s. The synthesized ID-Cu, OD-Cu, CD-Cu, BD-Cu, a graphite rod, and a Hg/HgO electrode (1 M KOH) were utilized as the working, counter, and reference electrodes, respectively. The anode and cathode chambers were separated by a Nafion membrane. The recorded potential was normalized with respect to the reversible hydrogen electrode (RHE) according to the following procedure:

$$E_{RHE}=E^{\ominus}(Hg/HgO) + 0.059\times pH+ 0.098. \quad (1)$$

ECSA was studied based on the electrochemical double-layer capacitance of various electrocatalysts at non-faradaic overpotentials. By plotting the difference of j between the anodic and cathodic sweeps (ja–jc) at 0.08 V vs. RHE against the scan rate, a linear trend was observed. The slope of the fitting line is equal to twice the geometric double layer capacitance (C_{dl}). The specific capacitance (C_s) for a flat surface is normally taken to be 40 μF/cm^2. Generally, the ECSA of the catalyst can be calculated by the following function:

$$ECSA = C_{dl}/C_s \quad (2)$$

2.3 HPLC analysis

HPLC (1260 Infinity II) with a UV detector was used to analyze HMF oxidation liquid phase products. The UV detector was adjusted to a wavelength of 265 nm. The mobile phase for HPLC was a mixture of ammonium formate and methanol, and the

flow rate was1 mL/min. A 4.6 mm×350 mm C18 column was used. The electrolyte was diluted to pH=13 before HPLC analysis. The quantification of HMF and its oxidation product was calculated based on the calibration curves of standard compounds with known concentrations. The FE of products was calculated on the basis of the following equations:

$$\text{Faraday efficiency (\%)} = n_{\text{experimentally produced}} / n_{\text{theoretically produced}} \times 100 \quad (3)$$

where n is the mole number of the substrate. The theoretically produced amount was calculated based on

$$n_{\text{theoretically produced}} = Q/(n \times F) \quad (4)$$

where Q is the transferred charge, n is the number of electrons transferred for each product molecule and F is Faraday's constant (96485 C/mol).

Selectivity (%) = 100% × n (a certain product) /n (all the detected products)

2.4 DFT calculations

We have employed the Vienna Ab Initio Package (VASP)[1]to perform all spin-polarized density functional theory (DFT) calculations within the generalized gradient approximation (GGA) using the Perdew-Burke-Ernzerhof (PBE)[2] formulation. We have chosen the projected augmented wave (PAW) potentials[3, 4]to describe the ionic cores and take valence electrons into account using a plane wave basis set with a kinetic energy cutoff of 450 eV. Partial occupancies of the Kohn−Sham orbitals were allowed using the Gaussian smearing method and a width of 0.05 eV. Electronic

energy was considered self-consistent when the energy change was smaller than 10^{-5} eV. Geometry optimization was considered convergent when the force change on each atom was smaller than 0.02 eV $Å^{-1}$. The vacuum spacing in a direction perpendicular to the plane of the structure is 18 Å. The weak interaction was described by DFT+D3 method using empirical correction in Grimme's scheme[5]. When performing the calculation, we fixed the atoms in the bottom two layers and allowed the relaxation of other atoms for structural optimization. To consider the strong correlation effects of transition metal in structure, all calculations were carried out by using the spin-dependent GGA plus Hubbard correction U method[6], and the effective Ueff parameters are 4.0 eV for Cu in model2(Cu-O(111)) and model3(Stretched Cu-O(111)). The Dipole correction taken into account for this calculation.

The Gibbs free energy change (ΔG) of each chemical reaction was calculated by Eq. 1,

$$\Delta G=\Delta E+\Delta ZPE-T\Delta S \quad (1)$$

where E is the calculated total energy, ZPE is the zero-pointenergy, T is the temperature, and S is the entropy.

Supply Figures

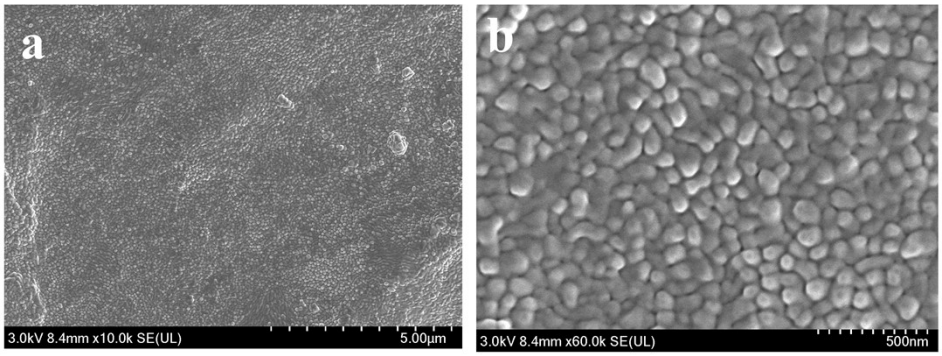

Figure S1. SEM images of CP.

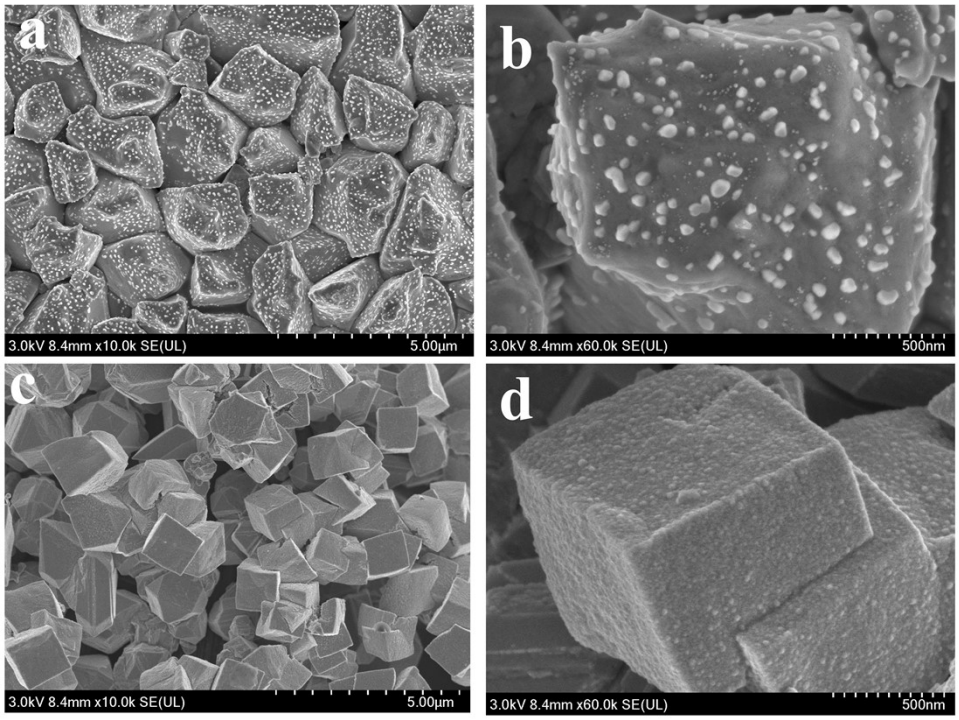

Figure S2. SEM images of (a-b) CuCl-CP and (c-d) CD-Cu-CP.

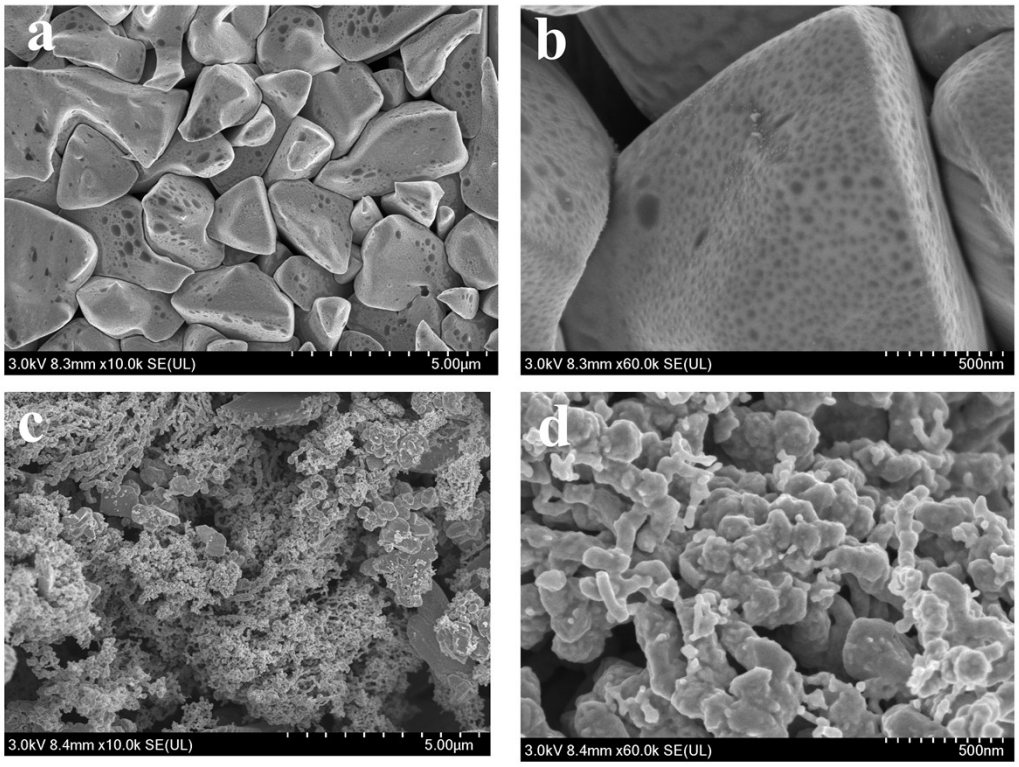

Figure S3. SEM images of (a-b) CuBr-CP and (c-d) BD-Cu-CP.

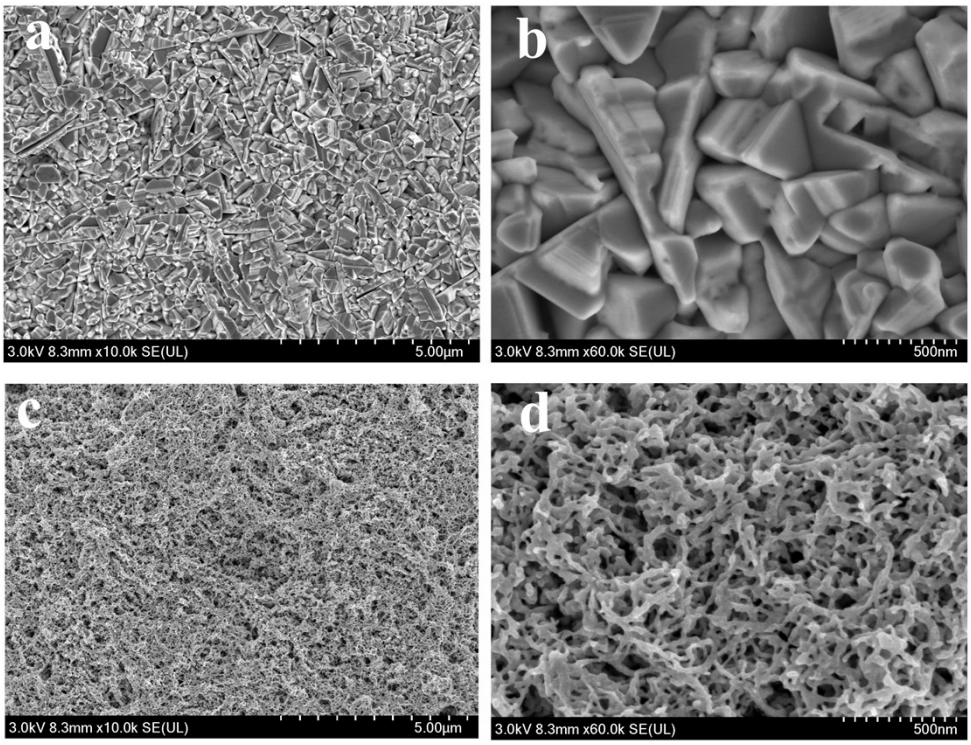

Figure S4. SEM images of (a-b) CuI-CP and (c-d) ID-Cu-CP.

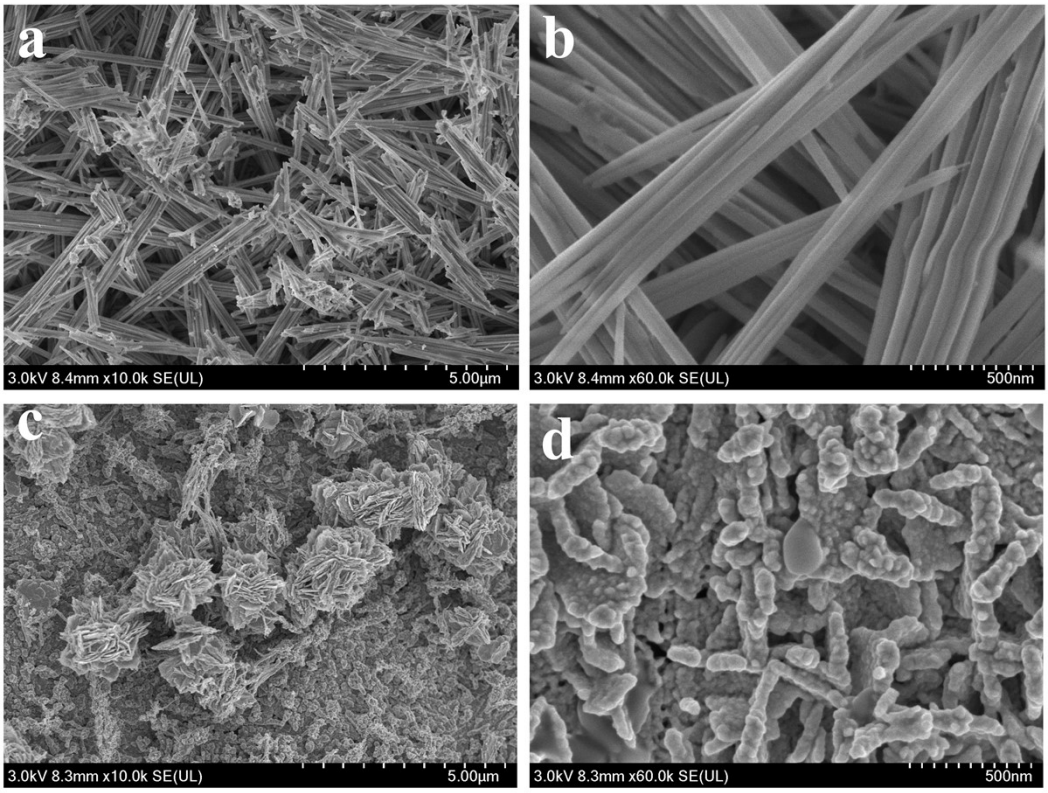

Figure S5. SEM images of (a-b) CuOH-CP and (c-d) OD-Cu-CP.

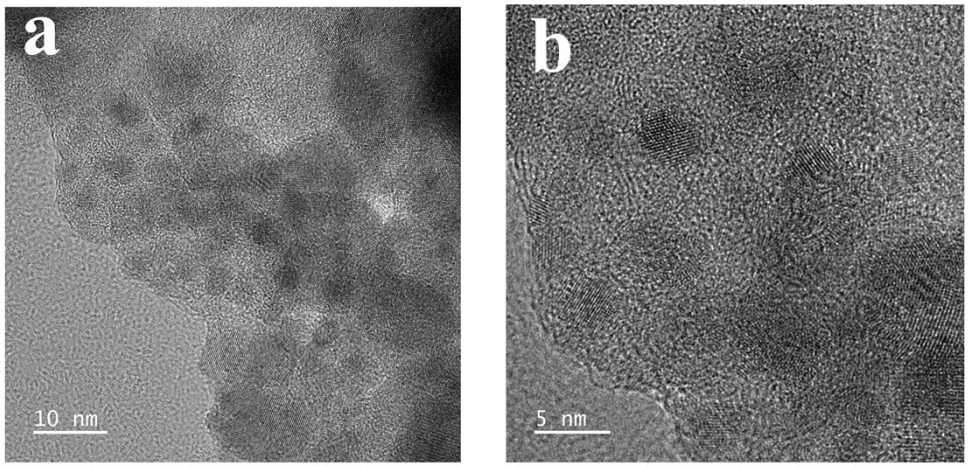

Figure S6. TEM images of ID-Cu-6.4%s.

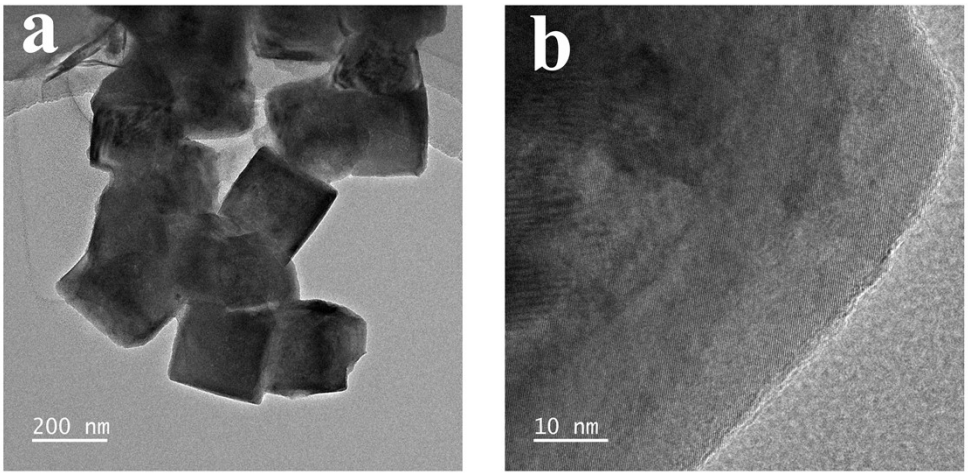

Figure S7. TEM images of CD-Cu.

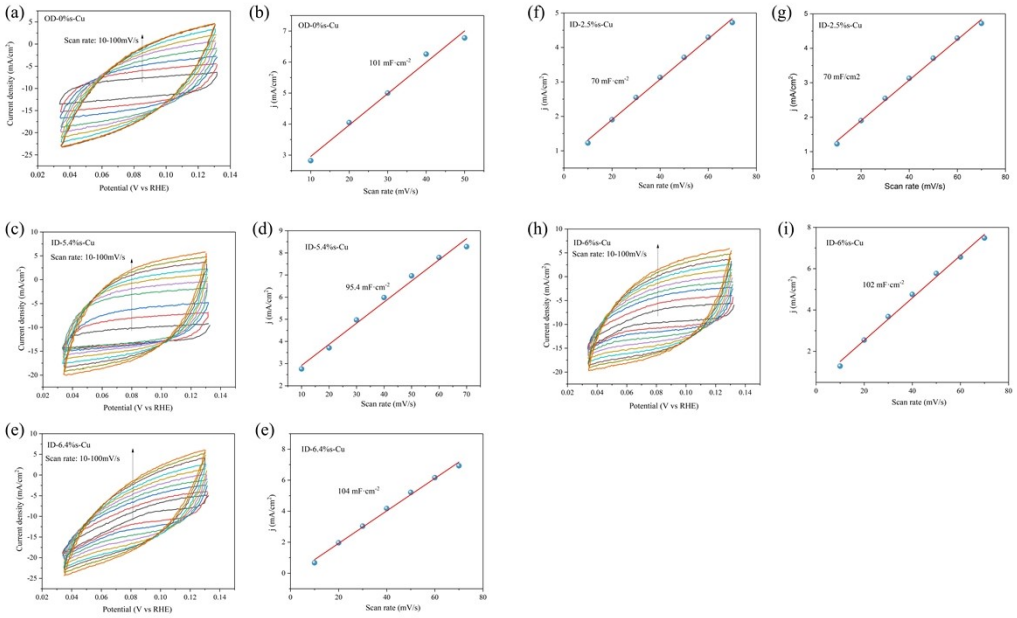

Figure S8. Capacitive currents at 0.08 V vs RHE as a function of the scan rate for (a) OD-0%s-Cu, (c) ID-5.4%s-Cu, (e) ID-6.4%s-Cu, (f) ID-2.5%s-Cu and (h) ID-6%s-Cu. CV curves for (b) OD-0%s-Cu, (d) ID-5.4%s-Cu, (e) ID-6.4%s-Cu, (g) ID-2.5%s-Cu and (i) ID-6%s-Cu.

Assuming that the active site density of the flat Cu electrode used in this study is 10^{15}. According by TOF calculation formula, the TOF value of ID-6.4%s-Cu is $0.07A/(1\times10^{15}\times2600 \text{ sites}\times96485 \text{ C mol}^{-1})=0.07\times6.022\times10^{23}/(1\times10^{15}\times2600 \text{ sites}\times96485 \text{ C mol}^{-1})=0.168 \text{ s}^{-1}$. In the same way, we can calculate the TOF value of ID-6%s-Cu, ID-5.4%s-Cu, ID-2.5%s-Cu and OD-0%s-Cu are 0.11 s^{-1}, 0.13 s^{-1}, 0.09 s^{-1} and 0.02 s^{-1}, respectively. Thus, tensile strain accelerated the HMFOR reactions in unit time and unit active site on Cu electrode, significantly improved HMFOR activity.

.

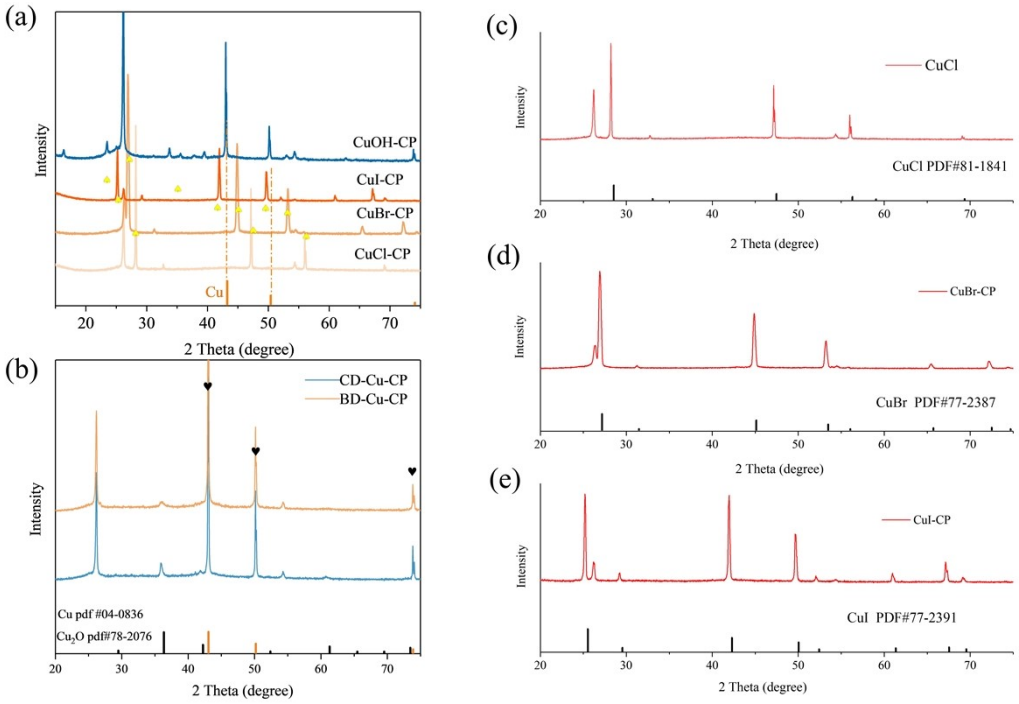

Figure S9. XRD patterns of (a, c-e) CuCl-CP, CuBr-CP, CuI-CP and CuOH-CP. XRD patterns of (b) CD-Cu-CP and BD-Cu-CP.

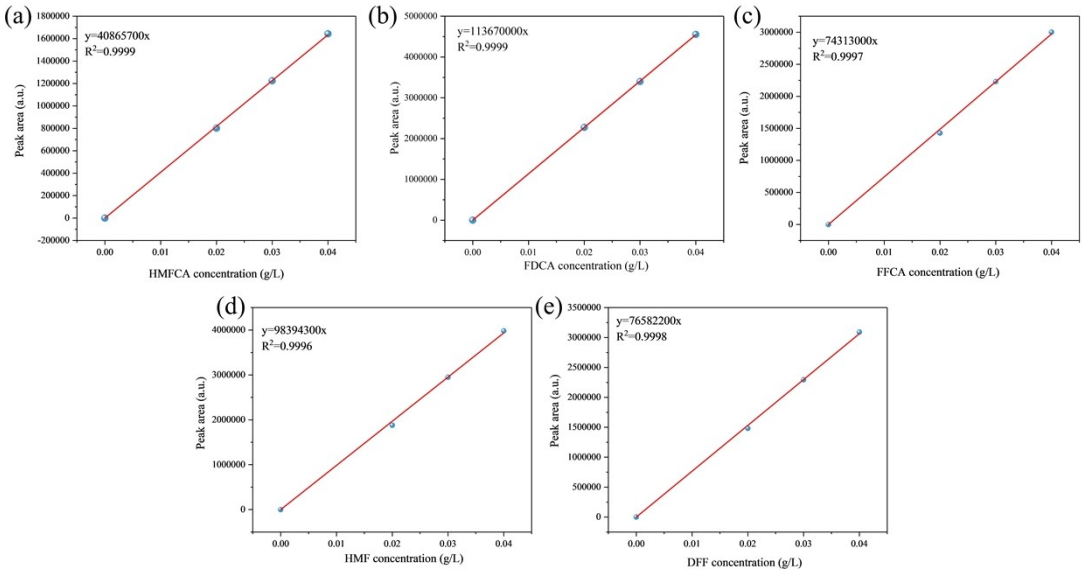

Figure S10. Calibration of the HPLC for (a) HMFCA. (b) FDCA. (c) FFCA. (d) HMF. (e) DFF.

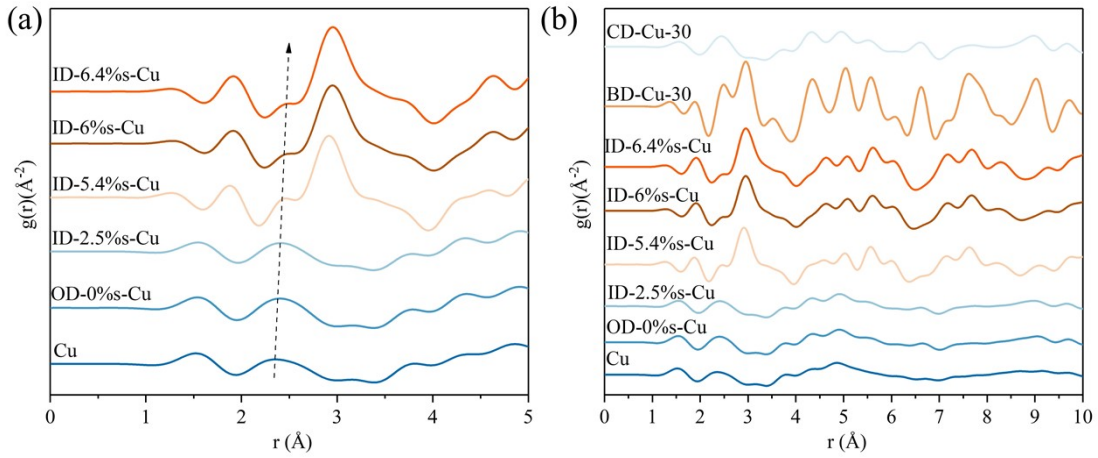

Figure S11. Pair distribution function (PDF) data of OD-0%s-Cu, ID-2.5%s-Cu, ID-5.4%s-Cu, ID-6%s-Cu, ID-6.4%s-Cu, CD-Cu and BD-Cu. Pair distribution function (PDF) can better capture the change of bond length and crystal information of Cu sites. As shown in Figure S11(a), the pure Cu has the Cu-Cu bond of 2.3Å, the Cu-Cu bond value of OD-0%s-Cu is same as pure Cu, illustrating the same structure of single Cu of OD-0%s-Cu. As the degree of iodination increasing, the tensile degree of Cu lattice is enhanced, resulting the Cu-Cu bond of ID-6.4%s-Cu increased to 2.5 Å compared to the 2.35 Å of ID-2.5%s-Cu. Figure S11(b) shows that CD-Cu-30 has the similar crystalline structure as pure Cu, while BD-Cu has the similar crystalline structure as ID-6.4%s-Cu, which contains some coordination environment of Cu-O.

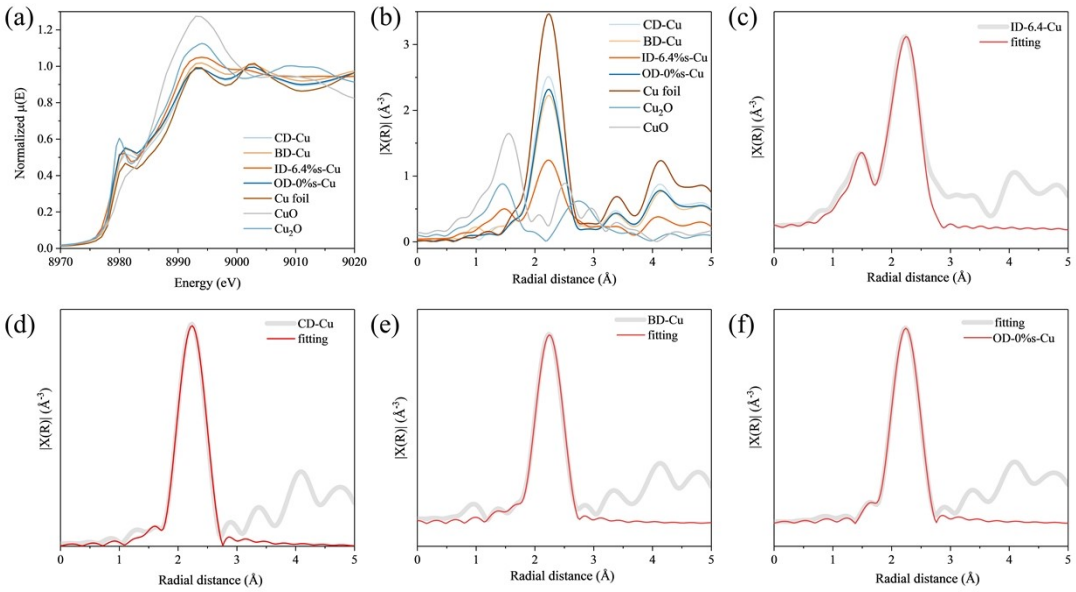

Figure S12. (a) Cu K-edge XANES spectra and (b corresponding FT EXAFS spectra of of ID-6.4%s-Cu, BD-Cu, CD-Cu, OD-0%s-Cu, BD-Cu, CD-Cu, Cu foil, CuO and Cu_2O. Fitted FT EXAFS spectra of (c) ID-6.4%s-Cu, (d) CD-Cu, (e) BD-Cu, (f) OD-0%s-Cu.

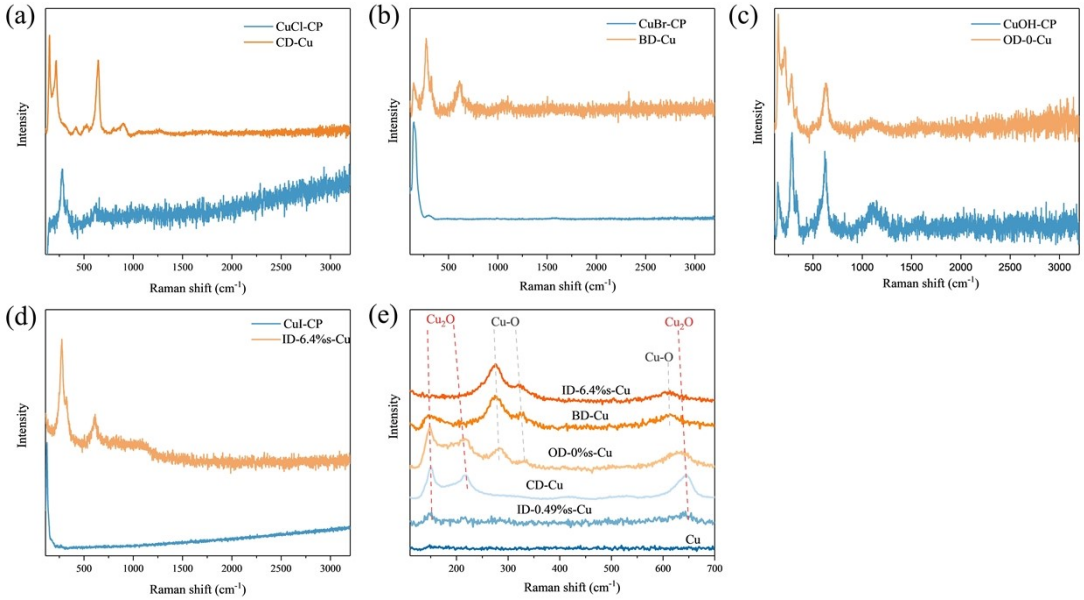

Figure S13. Raman spectra of (a) CuCl-CP and CD-Cu, (b) CuBr-CP and BD-Cu, (c) CuOH-CP and OD-0%s-Cu, (d) CuI-CP and ID-6.4%s-Cu. (e) Raman spectra of Cu, CD-Cu, BD-Cu, OD-0%s-Cu and ID-6.4%s-Cu.

As shown in Figure S13(a-d), the Cu-I, Cu-Br, Cu-Cl bond present at 125cm^{-1}, 176cm^{-1} and 230cm^{-1}, respectively[7-10]. After electro-reduction, OD-Cu, ID-Cu, BD-Cu and CD-Cu show the characteristics of Cu-O bond[11]. With the increase of lattice tensile strain of Cu, the mode of Cu-O bond (280cm^{-1}) is gradually dominated, which corresponds to the unsaturated Cu coordination.

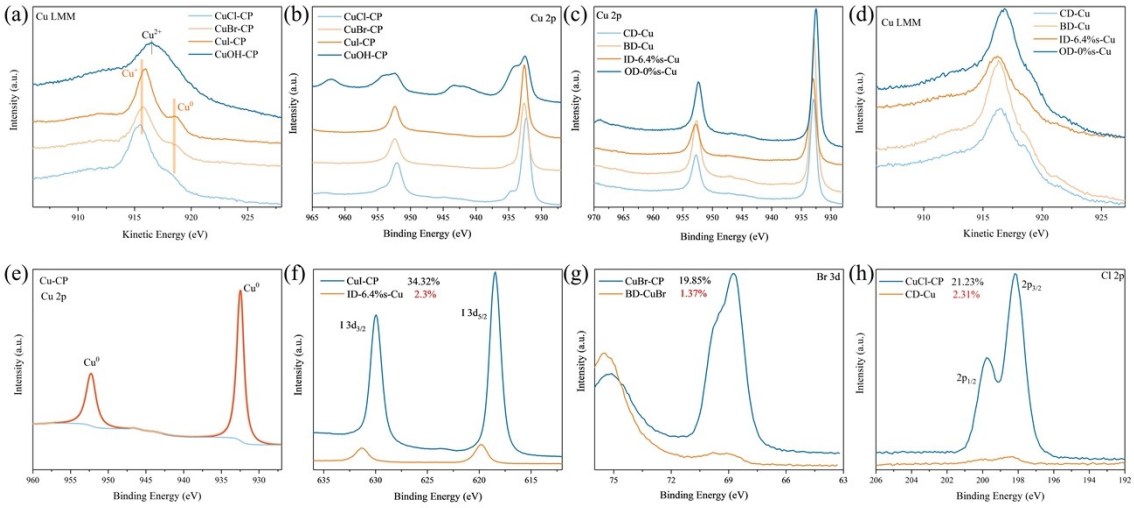

Figure S14. Auger electron spectra of (a) CuCl, CuBr, CuI, CuOH and (d) CD-Cu, BD-Cu, ID-6.4%s-Cu, OD-0%s-Cu. XPS spectra of (b) CuCl, CuBr, CuI, CuOH and (c) CD-Cu, BD-Cu, ID-6.4%s-Cu, OD-0%s-Cu. XPS spectra of (e) Cu. XPS spectra of (f) I element, (g) Br element and (h) Cl element.

The Cu 2p spectrum of pure Cu-CP is presented in Figure S14(e). The peak observed at 932.5 eV corresponds to Cu $2p_{3/2}$ of Cu^0, and the absence of a satellite peak indicates the lack of Cu^{2+} species. Figure S14(a) displays the Cu LMM spectra of CuX (X = Cl, Br, I), showing a main peak near 916 eV attributable to Cu^+. The narrow-scan Cu 2p spectra of these samples are shown in Figure S14(b), all exhibiting a characteristic peak at approximately 932.6 eV, which is also consistent with Cu^+. In contrast, both the Cu LMM and Cu 2p spectra of CuOH-CP confirm the presence of Cu^{2+}. Following electroreduction, the XD-Cu (X = Cl, Br, I, OH) samples exhibit spectral features indicative of mixed Cu^0 and Cu^+ states. Specifically, a Cu^0 peak emerges at around 918 eV in the Cu LMM spectra, while the Cu 2p spectra shows a single peak near 933 eV. Figure S14(f) presents the I 3d XPS spectra. For pristine CuI, the peak at 618 eV is assigned to I^-. After electroreduction, the intensity of the I signal

decreases substantially, accompanied by a peak shift, suggesting gradual leaching of iodine during the reduction process. The XPS spectra of Br and Cl are shown in Figure S14(g) and (h), respectively. Peaks at approximately 70 eV (Br $3d_{5/2}$) and 198.5 eV (Cl $2p_{3/2}$) are observed for the halide precursors. Their significant attenuation after reduction further supports the conversion of copper halides to metallic Cu^0.

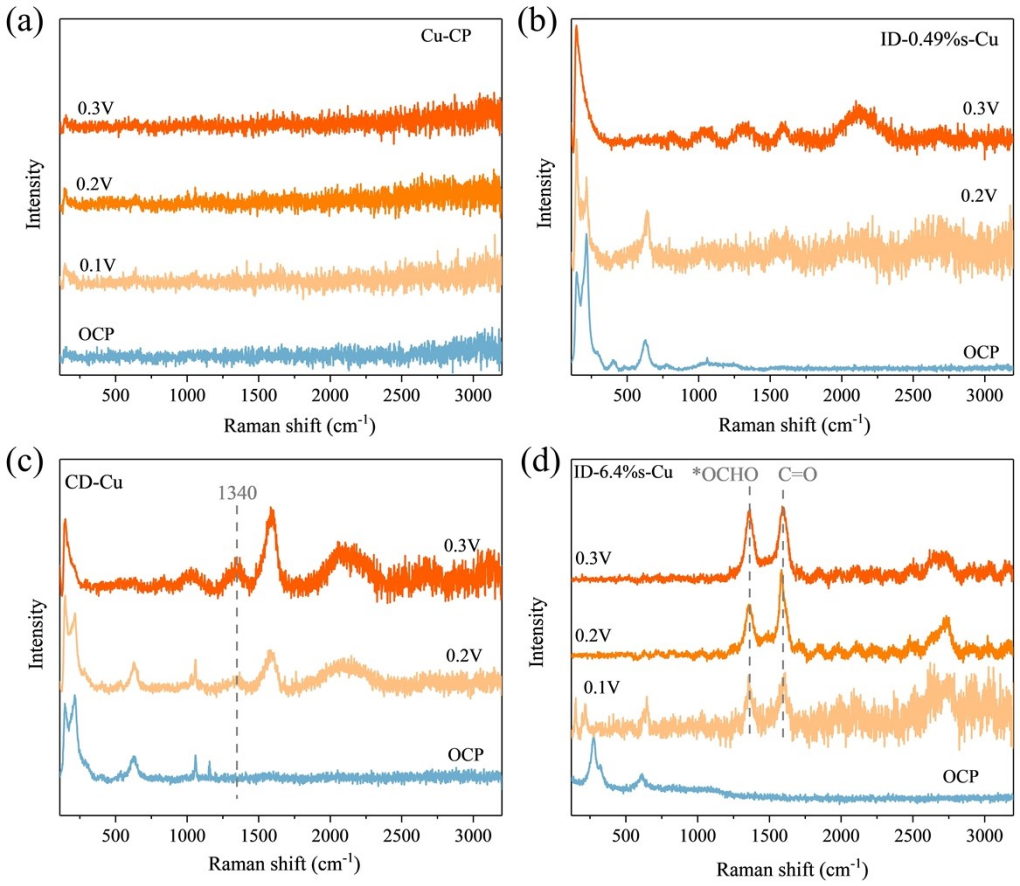

Figure S15. In situ Raman spectra in an electrolyte of 1.0 M KOH and 0.05 M HMF solution at different voltages of (a) Cu-CP, (b) ID-0.49%-Cu, (c) CD-Cu and (d) ID-6.4%s-Cu.

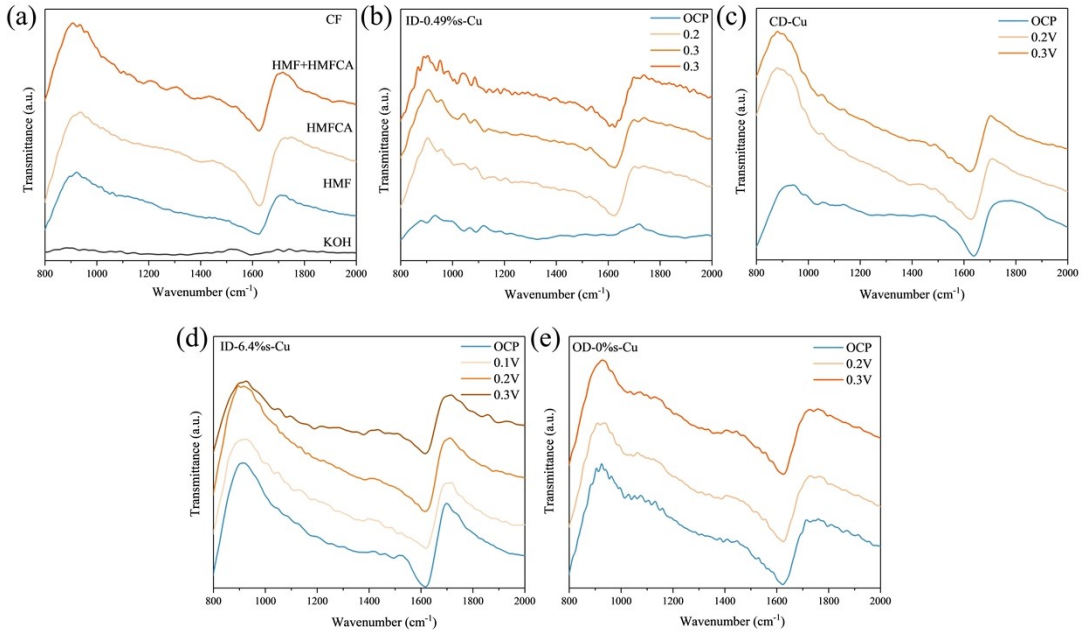

Figure S16. (a) In situ FTIR spectra of CF in KOH, HMF, HMFCA, mixed HMF and HMFCA solution. In situ FTIR spectra of (b) ID-0.49%s-Cu, (c) CD-Cu, (d) ID-6.4%s-Cu and OD-0%s-Cu in an electrolyte of 1.0 M KOH and 0.05 M HMF solution at different voltages.

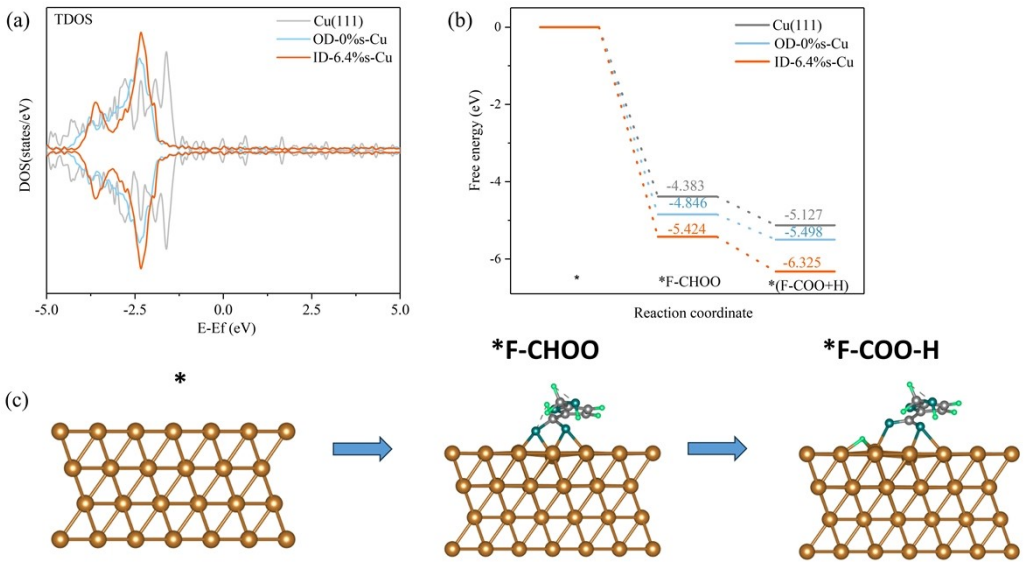

Figure S17. Theoretical determination of the essential HMF oxidation reaction pathway. (a) Calculated density of states of Cu(111), OD-0%s-Cu and ID-6.4%s-Cu with respect to the Fermi level. (b) Free energy profiles of HMFOR on Cu(111), OD-0%s-Cu and ID-6.4%s-Cu on Cu(111) surface. The reaction pathway of HMFOR on Cu(111) based on DFT calculation.

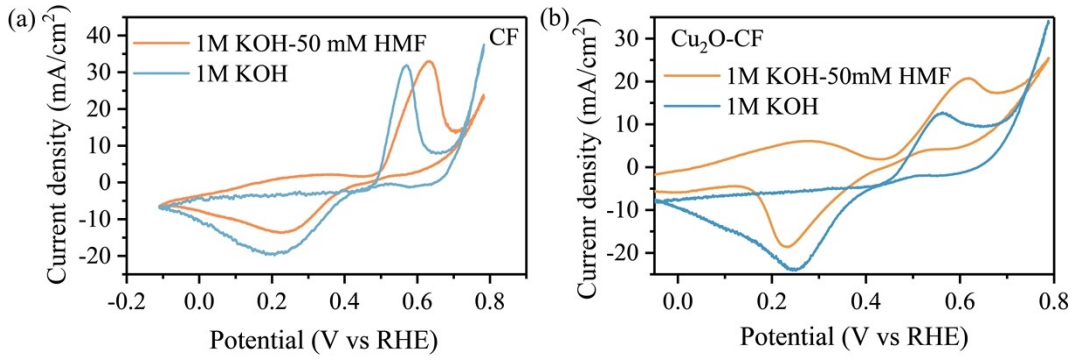

Figure S18. LSV curves of (a) CF and (b) Cu_2O-CF in 1M KOH with 50 mM HMF.

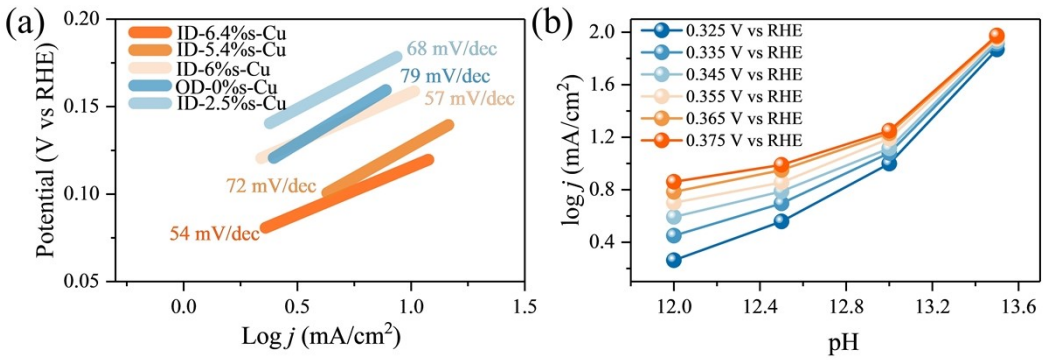

Figure S19. (a) Tafel slop of ID-6.4%s-Cu, ID-5.4%s-Cu, ID-6%s-Cu, OD-0%s-Cu and ID-2.5%s-Cu; (b) current-pH dependency of ID-6.4%s-Cu during various potential in 1M KOH with 50mM HMF.

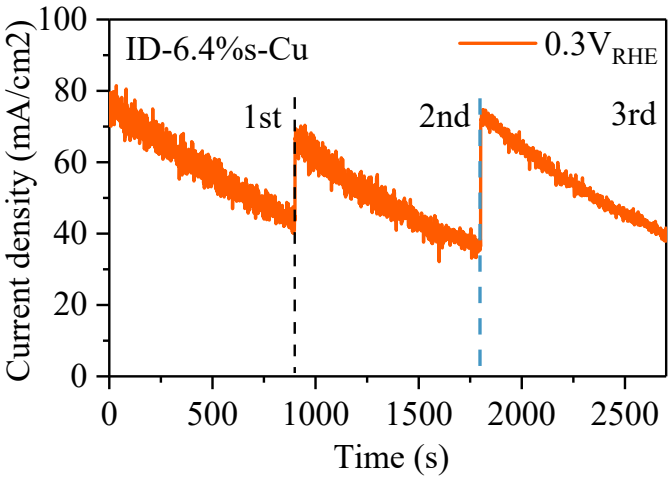

Figure S20. Cycling performance of ID-6.4%s-Cu under 0.3V vs RHE.

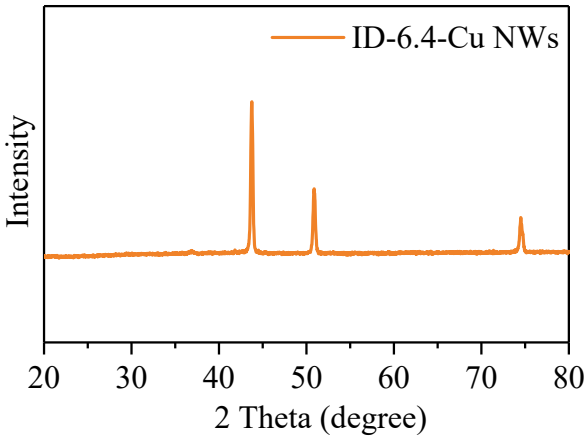

Figure S21. XRD patterns of ID-6.4%s-Cu NWs.

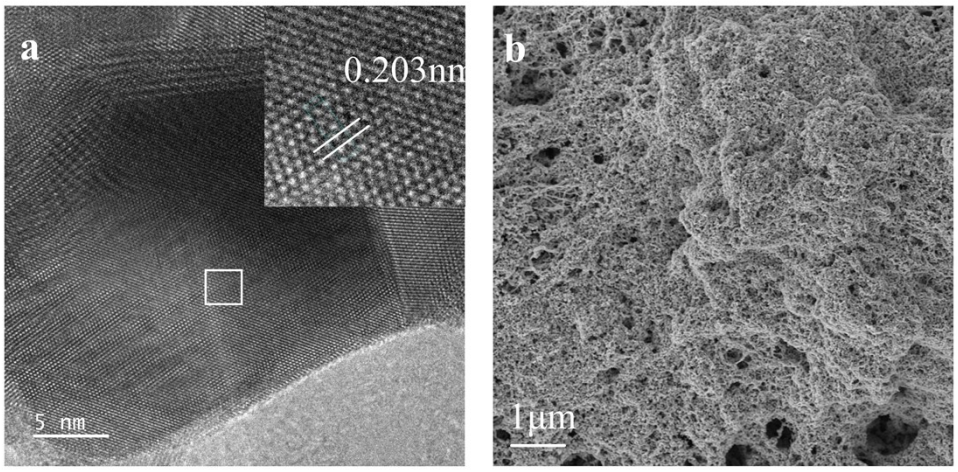

Figure S22. (a) HRTEM and (b) SEM images of ID-Cu(1min).

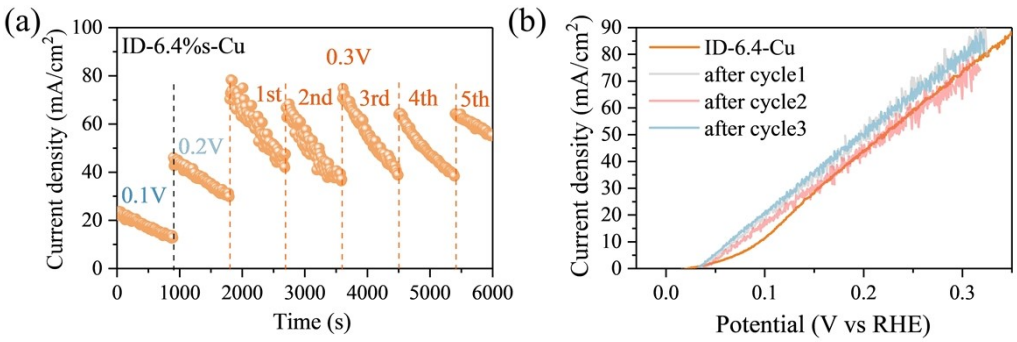

Figure S23. (a) Cycling performance of ID-6.4%s-Cu under 0.1V, 0.2V and 0.3V vs RHE. (b) LSV curves of ID-6.4%s-Cu after three cycles.

Table S1. EXAFS fitting parameters at the Cu K-edge for various samples.

Sample	**Shell**	**N**	**R(Å)**	**σ^2**	**R factor**
CD-Cu	Cu-Cu	11.4	2.539	0.0081	0.0057
	Cu-O	0.2	1.867	0.0032	
BD-Cu	Cu-Cu	9.4	2.543	0.0082	0.0064
	Cu-O	0.4	1.887	0.0022	
ID-6.4%s-Cu	Cu-Cu	6.4	2.544	0.0086	0.0374
	Cu-O	1.3	1.867	0.0032	
OD-0%s-Cu	Cu-Cu	10.53	2.538	0.0081	0.005

N: coordination numbers; R(Å): bond distance; σ^2: Debye-Waller factors; R factor: goodness of fit.

Table S2. Ion chromatography of CD-Cu, BD-Cu, ID-Cu.

Concentration / Samples	Cl, mg/g	Br, mg/g	I, mg/g
CD-Cu	0.2866	/	/
BD-Cu	/	119.2719	/
ID-Cu	/	/	3.722755

Table S3. HPLC performance of OD-0%s-Cu, ID-6.4%s-Cu, ID-2.5%s-Cu, ID-6%s-Cu

Samples \ Performance	HMF conversion rate (%)	HMFCA yield (%)	HMFCA formation rate (mmol h^{-1})
OD-0%s-Cu	8.6	5.97	0.59
ID-2.5%s-Cu	15.5	9.24	0.77
ID-6%s-Cu	17.3	10.12	0.85
ID-6.4%s-Cu	19.6	10.97	0.92

HMF conversion (%) = [n (HMF consumed)/n (HMF initial)] ×100

HMFCA yield (%) = [n (HMFCA formed)/ n (HMF initial)] ×100

HMFCA formation rate (mmol h^{-1})= n (HMFCA formed)/ Time

Table S4 Summary of the low potential organic oxidation performance by Cu-based catalysts in 1M KOH.

Anode	Oxidation substrate	Onset potential @ 1 mA/cm^2 (V)	Current density @ 0.3V vs RHE (mA/cm^2)	Ref
Cu	1M HCHO	0.025	12	[12]
Cu_2O	1M CH_3CHO	0.5	50	[12]
PtCu	0.2M FF	0.04	150	[13]
CF@Cu-NS	0.05M HCHO	-0.07	85	[14]
CuAgglv/Cu	0.2M FF	0.11	18	[15]
OD-Cu	0.2M FF	0.14	16	[15]
Cu NPs/Cu	0.2M FF	0.21	3	[15]
MV Cu	0.05M FF	0.02	115	[16]
Cu-modified glass carbon	0.05M HMF	0.15	0.7	[17]

Cu-modified glass carbon	0.05M FF	0.25	1.9	[17]
Cu_xO@CF	0.1M HCHO	-0.05	150	[18]
CF	0.1M HCHO	0.15	20	[18]
CuAu	0.2M FF	0.12	80	[19]
CuAg	0.2M FF	0.07	75	[19]
CuPd	0.2M FF	0.05	77	[19]
CF	0.2M FF	0.16	6	[19]
Cu	0.05M FF	0.02	123	[20]
Rh_1Cu	0.03M FF	0.01	60	[21]
Cu needles	0.05M HMF	0.05	8	[22]
An-Cu_2O-AC NWAs	0.05M HMF	0.03	115	[23]
$Cu(OH)_2$/CF	0.1M FF	0.15	50	[23]
Cu/CF	0.03M BzH	0.12	12.5	[24]
Cu_xO/CF	0.03M BzH	0.06	45	[24]
Ag-Cu_xO/CF	0.03M BzH	0.04	74	[24]

ID-6.4%s-Cu NWs(3)	*0.125M HMF*	*0*	*180*	*This work*

Table S5. HPLC performance of ID-6.4%s-Cu (CF) under three cycles.

Performance / Samples	HMF conversion rate (%)	HMFCA yield (%)	FEHMFCA (%)	Selectively (%)
ID-6.4%s-Cu (Cycle1)	34.9	22.5	103.8	100
ID-6.4%s-Cu (Cycle2)	33.5	20.1	102.3	100
ID-6.4%s-Cu (Cycle3)	33.9	21	100.5	100

References

(1) Kresse, G.; Furthmüller, J. Efficiency of ab-initio total energy calculations for metals and semiconductors using a plane-wave basis set. *Computational Materials Science* **1996**, *6* (1), 15-50. DOI: https://doi.org/10.1016/0927-0256(96)00008-0.

(2) Perdew; Burke; Ernzerhof. Generalized Gradient Approximation Made Simple. *Physical review letters* **1996**, *77* (18), 3865-3868, Journal Article. DOI: 10.1103/PhysRevLett.77.3865.

(3) Kresse, G.; Joubert, D. From ultrasoft pseudopotentials to the projector augmented-wave method. *PHYSICAL REVIEW B* **1999**, *59* (3), 1758-1775, Article. DOI: 10.1103/PhysRevB.59.1758.

(4) Blochl. Projector augmented-wave method. *Physical review. B, Condensed matter* **1994**, *50* (24), 17953-17979, Journal Article. DOI: 10.1103/PhysRevB.50.17953.

(5) Grimme, S.; Antony, J.; Ehrlich, S.; Krieg, H. A consistent and accurate ab initio parametrization of density functional dispersion correction (DFT-D) for the 94 elements H-Pu. *JOURNAL OF CHEMICAL PHYSICS* **2010**, *132* (15), Article. DOI: 10.1063/1.3382344.

(6) Grimme, S.; Antony, J.; Ehrlich, S.; Krieg, H. A consistent and accurate ab initio parametrization of density functional dispersion correction (DFT-D) for the 94 elements H-Pu. *The Journal of Chemical Physics* **2010**, *132* (15), 154104. DOI: 10.1063/1.3382344.

(7) Tan, C.-S.; Chen, H.-Y.; Chen, H.-S.; Gwo, S.; Chen, L.-J. Intermediates in the cation reactions in solution probed by an in situ surface enhanced Raman scattering method. *Scientific Reports* **2015**, *5* (1), 13759. DOI: 10.1038/srep13759.

(8) Hole, A.; Tyagi, G.; Sahu, A.; Shaikh, R.; Krishna, C. M. Exploration of Raman exfoliated cytology for oral and cervical cancers. *Vibrational Spectroscopy* **2018**, *98*, 35-40. DOI: https://doi.org/10.1016/j.vibspec.2018.07.001.

(9) Bushiri, M. J.; Antony, C. J.; Fleck, M. Raman and infrared spectral studies of [C(NH2)3]2MII(H2O)4(SO4)2, MII = Mn, Cd and VO. *Journal of Raman Spectroscopy* **2008**, *39* (3), 368-373. DOI: https://doi.org/10.1002/jrs.1828.

(10) Edis, Z.; Bloukh, S. H. Antimicrobial V-Shaped Copper(II) Pentaiodide: Insights to Bonding Pattern and Susceptibility. In *Molecules*, 2022; Vol. 27, p 6437.

(11) Lei, Q.; Huang, L.; Yin, J.; Davaasuren, B.; Yuan, Y.; Dong, X.; Wu, Z.-P.; Wang, X.; Yao,

K. X.; Lu, X.; et al. Structural evolution and strain generation of derived-Cu catalysts during CO2 electroreduction. *Nature Communications* **2022**, *13* (1), 4857. DOI: 10.1038/s41467-022-32601-9.

(12) Xiao, L.; Dai, W.; Mou, S.; Wang, X.; Cheng, Q.; Dong, F. Coupling electrocatalytic cathodic nitrate reduction with anodic formaldehyde oxidation at ultra-low potential over Cu2O. *Energy & Environmental Science* **2023**, *16* (6), 2696-2704, 10.1039/D3EE00635B. DOI: 10.1039/D3EE00635B.

(13) Zhang, X.; Zhu, W.; Zhou, H.; Sun, L.; Wang, Z.; Liang, H. An acid-alkaline furfural hybrid battery for furoate and bipolar hydrogen production. *Chemical Communications* **2023**, *59* (45), 6837-6840, 10.1039/D3CC00936J. DOI: 10.1039/D3CC00936J.

(14) Yang, Y.; Wu, X.; Ahmad, M.; Si, F.; Chen, S.; Liu, C.; Zhang, Y.; Wang, L.; Zhang, J.; Luo, J.-L.; et al. A Direct Formaldehyde Fuel Cell for CO2-Emission Free Co-generation of Electrical Energy and Valuable Chemical/Hydrogen. *Angewandte Chemie International Edition* **2023**, *62* (21), e202302950. DOI: https://doi.org/10.1002/anie.202302950.

(15) Liu, H.; Agrawal, N.; Ganguly, A.; Chen, Y.; Lee, J.; Yu, J.; Huang, W.; Mba Wright, M.; Janik, M. J.; Li, W. Ultra-low voltage bipolar hydrogen production from biomass-derived aldehydes and water in membrane-less electrolyzers. *Energy & Environmental Science* **2022**, *15* (10), 4175-4189, 10.1039/D2EE01427K. DOI: 10.1039/D2EE01427K.

(16) Yang, M.; Li, Y.; Dong, C.-L.; Li, S.; Xu, L.; Chen, W.; Wu, J.; Lu, Y.; Pan, Y.; Wu, Y.; et al. Correlating the Valence State with the Adsorption Behavior of a Cu-Based Electrocatalyst for Furfural Oxidation with Anodic Hydrogen Production Reaction. *Advanced Materials* **2023**, *35* (39), 2304203. DOI: https://doi.org/10.1002/adma.202304203.

(17) Wang, T.; Tao, L.; Zhu, X.; Chen, C.; Chen, W.; Du, S.; Zhou, Y.; Zhou, B.; Wang, D.; Xie, C.; et al. Combined anodic and cathodic hydrogen production from aldehyde oxidation and hydrogen evolution reaction. *Nature Catalysis* **2022**, *5* (1), 66-73. DOI: 10.1038/s41929-021-00721-y.

(18) Pan, Y.; Li, Y.; Dong, C.-L.; Huang, Y.-C.; Wu, J.; Shi, J.; Lu, Y.; Yang, M.; Wang, S.; Zou, Y. Unveiling the synergistic effect of multi-valence Cu species to promote formaldehyde oxidation for anodic hydrogen production. *Chem* **2023**, *9* (4), 963-977. DOI: 10.1016/j.chempr.2022.12.008.

(19) Liu, H.; Yu, J.; Chen, Y.; Lee, J.; Huang, W.; Li, W. Cu-Based Bimetallic Catalysts for

Electrocatalytic Oxidative Dehydrogenation of Furfural with Practical Rates. *ACS Applied Materials & Interfaces* **2023**, *15* (31), 37477-37485. DOI: 10.1021/acsami.3c06783.

(20) Liu, S.-Q.; Xie, S.; Wu, S.; Yang, Y.; Lei, P.-X.; Luo, S.; Feng, R.; Fu, X.-Z.; Luo, J.-L. Self-Powered System for H2 Production and Biomass Upgrading. *Advanced Functional Materials* **2024**, *34* (41), 2404105. DOI: https://doi.org/10.1002/adfm.202404105.

(21) Li, J.; Ji, K. Y.; Li, B. Y.; Xu, M.; Wang, Y.; Zhou, H.; Shi, Q. J.; Duan, H. H. Rechargeable Biomass Battery for Electricity Storage/generation and Concurrent Valuable Chemicals Production. *ANGEWANDTE CHEMIE-INTERNATIONAL EDITION* **2023**, *62* (31). DOI: 10.1002/anie.202304852.

(22) Fu, G.; Kang, X.; Zhang, Y.; Guo, Y.; Li, Z.; Liu, J.; Wang, L.; Zhang, J.; Fu, X.-Z.; Luo, J.-L. Capturing critical gem-diol intermediates and hydride transfer for anodic hydrogen production from 5-hydroxymethylfurfural. *Nature Communications* **2023**, *14* (1), 8395. DOI: 10.1038/s41467-023-43704-2.

(23) Wu, B.; Wei, G.; Zhu, P.; Huang, Q.; Wang, L.; Yuan, K.; Li, L.; Chen, Y. Unlocking Dual-Pathway Low-Potential Aldehyde Oxidation on Chromium-Doped Copper Catalysts. *Angewandte Chemie International Edition* **2026**, *65* (6), e25384. DOI: https://doi.org/10.1002/anie.202525384.

(24) Xie, Z.; Zu, X.; Lai, Q.; Cao, Y.; Qiu, X. Electricity generation coupled with hydrogen production at room temperature by lignin-derived aldehyde flow fuel cell based on Ag-CuxO/CF electrocatalyst. *Applied Catalysis B: Environment and Energy* **2026**, *383*, 126054. DOI: https://doi.org/10.1016/j.apcatb.2025.126054.